Contents

1 Introduction **3**

2 An introduction to the theory of radar interferometry **3**

2.1 Basic principles 4

2.2 Interferogram 5

2.3 Coherence 6

2.4 Generation of interferometric products 7

2.5 Estimation of terrain height 9

2.6 Interferometric configurations 10

2.6.1 Across-track interferometry 10

2.6.2 Along-track interferometry 10

2.6.3 Repeat-pass interferometry 11

2.6.4 Differential interferometry 11

2.6.5 Interferometry and different SAR system parameters 11

3 Spaceborne and airborne sensors **12**

3.1 Airborne InSAR systems 12

3.2 Spaceborne sensors 12

3.2.1 SEASAT 12

3.2.2 SIR-C/X-SAR 12

3.2.3 SRTM 14

3.2.4 ERS 14

3.2.5 ENVISAT 14

3.2.6 Radarsat 14

4 A survey of applications **15**

4.1 Land-cover classification 15

4.2 Crop monitoring 15

4.3 Forestry 16

4.4 Digital elevation models 17

4.5 Monitoring of snow covered regions 20

4.6 Glacier motion measurements 20

4.7 Flood monitoring 20
4.8 Geophysical hazard analysis 22
4.8.1 Earthquake risk monitoring 22
4.8.2 Monitoring of volcanic activity 22
4.9 Geological applications 23
4.10 Other applications 23

5 Case study: analysis of Radarsat images from Heimdalen **23**

6 Conclusions **27**

1 Introduction

The use of spaceborne SARs as interferometers has recently become popular, but the basic principles date back to the early 1970s [Graham 74, Richman 71]. For terrestrial applications the first results were produced in the 1980s [Gabriel and Goldstein 88, Gabriel et al. 89, Goldstein et al. 89, Goldstein and Zebker 87, Goldstein et al. 88, Zebker and Goldstein 86]. For spaceborne applications, only a few data sets from the 1978 SEASAT mission were available. However, after the launch of the ERS-1 satellite in 1991 a large amount of data became available and the research on interferometry applications has had an enormous growth.

A radar interferometer is formed by relating signals from two antennas imaging the same area. Today, interferometric SAR (InSAR) is generally regarded as an extremely powerful tool for mapping the Earth's land, ice and even the sea surface topography. For recent review papers of SAR interferometry, see [Bamler and Hartl 98, Gens and van Genderen 96, Gabriel et al. 89]. Differential InSAR methods represent unique tools for detecting and mapping surface displacements over large temporal and spatial scales with precision in the centimeter and even millimeter range, given optimal conditions. The precision achieved for a particular data set depends on parameters like orbit accuracy, baseline, wavelength, SNR characteristics of the sensor, and the temporal correlation of the surface cover. InSAR data are important for applications like generation of Digital Elevation Models (DEM), earthquake and volcanic research, glaciology and ice sheet monitoring, monitoring of land subsidence due to mining, gas, water, and oil withdrawal etc. Repeat-pass interferometry allows the detection of changes of spatial and/or dielectric properties of the land surface, which can be used for land cover classification, mapping of flooded areas, monitoring of geophysical parameters etc.

In this report, we first review the basic principles of interferometric SAR. We shortly describe different InSAR sensors. The main application areas are then reviewed. A case study for analysing coherence for snow-covered regions is then presented.

2 An introduction to the theory of radar interferometry

The purpose of this section is to present the most basic principles of radar interferometry. The aim is to provide enough details to be able to understand the requirements and potential for different applications, without presenting the theory in depth.

A radar interferometer is formed by relating the signals from two antennas imaging the same area. This can be achieved either by two antennas on a single platform, or by repeated passes over the area by a single antenna. Both airborne and spaceborne sensors can be used.

In SAR imaging, the backscattering signal from a particular area is the coherent superposition of the backscattering from the individual scatterers within that cell, resulting in a random phase and the speckle phenomenon. For two SAR images acquired with almost identical antenna positions, the scatter geometries are almost identical and therefore the speckle patterns of the two images are not independent. The *interferometric phase*, i.e. the phase difference between these two images, is a measure of the difference in path lengths to the sensors. This allows the derivation of the three-dimensional position of the scattering element.

There are two basic interferometric data products, the *interferogram* and the *coherence image*. An interferogram is formed using the phase from two complex SAR images, while a coherence image is made by using both the amplitude and the phase from the SAR image pair. These are explained in section 2.2.

Two of the major applications of interferometric SAR, the derivation of height maps and differential

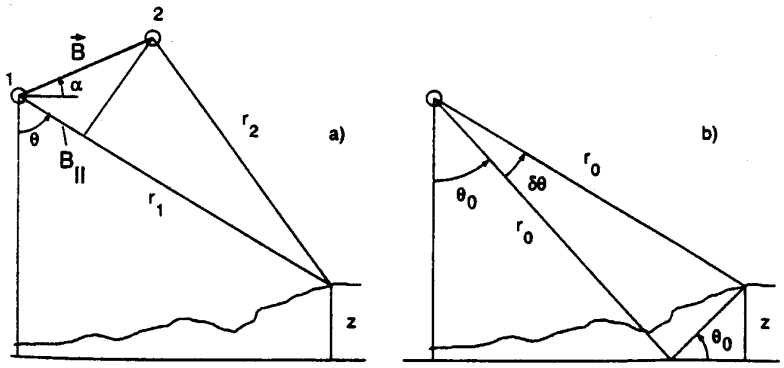

Figure 1: *Interferometric imaging geometry. (a) Two apertures separated by a baseline B are flying (in the direction into the paper) imaging a swath on the ground. (b) Conventions in linearizing the interferometer equation (Rosen et al. 96).*

displacement maps, are based on the geometric information contained in the interferogram. The quality of the products is characterized by the coherence, which is a measure of the variance of the interferometric phase estimate. The coherence can be said to be an estimate of the phase stability of the imaged targets in the time between two SAR acquisitions. If the surface is changing (e.g., due to soil moisture changes, vegetation growth and canopy changes, snow cover), the coherence will decrease. The coherence can also change if the object has a volumetric scattering component [Askne and Hagberg 93]. Although the coherence is often used merely to evaluate the quaility of the interferogram, it contains information in itself which can be very valuable for several other applications as discussed later.

2.1 Basic principles

A short introduction to the basic principles of interferometry has been adopted from [Rosen et al. 96]. Two imaging antennas (or antenna positions) separated by the baseline vector $\mathbf{B}$, depicted in Figure 1, are in motion perpendicular to the page, and represent the platform track(s). The phase at each point in a radar image is the sum of the backscatter phase ϕ_{bi} and the propagation phase $\phi_{pi} = -(4\pi/\lambda)r_i$, where r_i is the range from antenna i to the imaged point. For two radars imaging a scene at the same frequency and with similar viewing geometry, the backscatter phase will be nearly equal: $\phi_{b1} \approx \phi_{b2}$. Under these assumptions, the phase difference between the two images at a given point is

$$\Delta\phi = \phi_1 - \phi_2 = -\frac{4\pi}{\lambda}(r_1 - r_2). \tag{1}$$

For spaceborne geometries, where $|\mathbf{B}| \ll \mathbf{r}$, we may write

$$\Delta\phi = -\frac{4\pi}{\lambda}\mathbf{BI} = -\frac{4\pi}{\lambda}\mathbf{B}\sin(\theta - \alpha), \tag{2}$$

where $\mathbf{I}$ is a unit vector in the look direction. In words, the phase difference is proportional to the component of $\mathbf{B}$ in the look direction.

To see how this phase relates to topography, consider a surface without local topography. Then,

$$\Delta\phi_0 = -\frac{4\pi}{\lambda}B\sin(\theta_0 - \alpha), \tag{3}$$

where θ_0 is the look angle to a given point on the ground. If topography is present, the look angle for a given range will be altered by $\delta\theta$ as illustrated in Figure 1 (b):

$$\delta\phi = -\frac{4\pi}{\lambda} B \sin(\theta_0 + \delta\theta - \alpha). \tag{4}$$

The "flattened" phase differences, formed by removing the flat-Earth phase

$$\Delta\phi_{flat} = \Delta\phi - \Delta\phi_0 \approx -\frac{4\pi}{\lambda} B \cos(\theta_0 - \alpha) \tag{5}$$

is to first order proportional to the perpendicular component of the baseline $B_{\perp 0} = B\cos(\theta_0 - \alpha)$, and to the small angle $\delta\theta$, which in turn, is proportional to the topographic height z : $\delta\theta \approx z/r_0 \sin\theta_0$. The so-called ambiguity height is the elevation changes required to alter the phase difference by one cycle (2π) and is given by:

$$h_a = \frac{\lambda r_0 \sin\theta_0}{2B_{\perp 0}}. \tag{6}$$

The height ambiguity is often used to characterize the sensitivity of the interferometer.

The phase difference in repeat-pass observations measures any ground displacement in addition to topography. The range change in the second image Δr due to displacement enters into the phase difference directly:

$$\Delta\phi_{flat} = -\frac{4\pi}{\lambda} B \cos(\theta_0 - \alpha) \frac{z}{r_0 \sin\theta_0} + \frac{4\pi}{\lambda}\Delta r. \tag{7}$$

Note that the phase difference is far more sensitive to changes in topography (surface displacement) than to the topography itself. From Eq. (7), $\Delta r = \lambda/2$ gives one cycle of phase difference, while z must change by h_a to affect the same change.

A major problem in isolating motions from other phase modulations in an interferogram is the topography itself. Removing the topographic phase signature from an interferogram requires either a reference digital elevation model of sufficient resolution and accuracy, or an independent interferogram with no motion present. Using a DEM, one may synthesize an interferogram if the imaging geometry is known. Subtracting the phase differences pixel by pixel removes the topographic phase and leaves only the phase due to motion.

2.2 Interferogram

Consider the two complex SAR images $g_1(r,a)$ and $g_2(r,a)$, where r is the range position and a the azimuth position. The interferogram $v(r,a)$ is given by

$$v(r,a) = g_1(r,a)g_2^*(r,a) = |g_1(r,a)||g_2(r,a)| \exp^{j\Delta\phi(r,a)}, \tag{8}$$

where * denotes complex conjugation, and

$$\Delta\phi(r,a) = \phi_1(r,a) - \phi_2(r,a) \tag{9}$$

is the interferometric phase.

The probability distribution function of the magnitude and phase of an interferogram sample is given in [Bamler and Hartl 98, Lee et al. 94].

2.3 Coherence

The coherence γ is defined as the complex correlation coefficient (or coherence) between the two SAR images:

$$\gamma = \frac{E[g_1(r,a)g_2^*(r,a)]}{\sqrt{E[|g_1(r,a)|]^2 E[|g_2(r,a)|]^2}}. \tag{10}$$

The coherence magnitude $|\gamma|$ varies between zero (no correlation) and one (the images are equal). Its phase is the expected interferometric phase $\Delta\phi$ of the pixel, and its magnitude is related to the variance of the phase noise.

The coherence can be written as a product of the contribution from different factors [Weydahl 98]:

$$\gamma = \gamma_{SystemSNR}\gamma_{Processor}\gamma_{Baseline}\gamma_{Registration}\gamma_{Temporal} \tag{11}$$

In practice, the coherence is always less than one due to different decorrelation factors which are due to changes in imaging parameters. The quality of an interferometric image pair is often characterized in terms of the coherence magnitude. It is desirable to minimize these decorrelation factors. The system SNR decorrelation, $\gamma_{SystemSNR}$, is for satellite SAR data only a problem for areas with very low backscattering, like radar shadow or smooth water surfaces. The processing stages going from the SAR raw data to the single look complex SAR image can cause the decorrelation $\gamma_{Processor}$ due to defocusing in azimuth or range. The temporal decorrelation $\gamma_{Temporal}$ can be due to any change in the scattering mechanisms of the target, e.g., wind, soil moisture, snow, vegetation growth.

The spatial baseline decorrelation $\gamma_{Baseline}$ comes from the difference in imaging geometry between the two passes since the two antennas will observe a ground surface resolution element under slightly different viewing angles. The critical baseline and decorrelation factors can be estimated for different SAR parameter settings [Weydahl 98]. Larger baselines can be tolerated for RADARSAT than for ERS given the same decorrelation limits. The larger tolerance is a combined effect of larger range and finer resolution. The baseline decorrelation effect can be compensated for using a common spectral band filtering technique in the range direction [Gatelli et al. 94].

Baseline limitations The baseline is limited by the orbit navigation accuracy. Above a critical length of baseline (approximately 1100 m for ERS) there is a complete loss of coherence. The degree of coherence significantly influences the accuracy of the phase and hence all information derived from the interferogram (like, e.g., height measurements). In practice, there are limitations on length of baseline for which useful interferograms can be calculated. For mapping, the optimal baseline length for ERS is between 50 m and 300 m. Shorter baselines can yield useful information regarding glacier properties but tend not to yield useful data sets for height estimation. The upper practical limit for ERS is about 600 m.

Coherence estimation The coherence is estimated by spatial averaging of the complex pixel values $g_1(r,a)$ and $g_2(r,a)$ in the corresponding pixel (r,a) of image 1 and 2 after the SAR images have been co-registered with high accuracy ($< 1/10$ pixel size) [Monti Guarnieri and Prati 97]:

$$\bar{\gamma} = \left| \frac{\sum_{r=1}^{R}\sum_{a=1}^{A}\{g_1(r,a)g_2^*(r,a)\exp^{-j\Delta\phi(r,a)}\}}{\sqrt{\sum_{r=1}^{R}\sum_{a=1}^{A}|g_1(r,a)|^2 \sum_{r=1}^{R}\sum_{a=1}^{A}|g_2(r,a)|^2}} \right| \tag{12}$$

Note that even if all the scatterers within the estimation area are independent with identical

statistical properties, the two images differ by a deterministic phase (i.e., the interferometric phase $\Delta\phi(r,a)$), which should be estimated and compensated for.

Assuming flat topography the standard deviation of the sample coherence is given by [Monti Guarnieri and Prati 97]:

$$\sigma_{\bar{\gamma}} = \frac{1-\gamma^2}{\sqrt{2RA}}, \tag{13}$$

where RA is the number of independent samples (range, azimuth) that are used in the coherence estimation. Thus, we see that for low coherence areas, a large number of samples is needed to achieve acceptable estimation precision.

A window of size e.g. $R \times A$ pixels (range, azimuth) can be used. Normally, A is greater than R, e.g. $R = 5$ and $A = 25$. Larger windows will result in larger coherence estimates.

2.4 Generation of interferometric products

The generation of an interferometric image product is a fairly complex procedure. A schematic view is given in Figure 2. A typical procedure can be [Lanari et al. 96]:

- *Range and azimuth filtering of the complex images.* Before the interferogram is formed, the complex image pair has to be separately filtered in both range and azimuth to optimize the coherence and the interferometric phase purity. Range filtering is applied to minimize baseline-induced decorrelation. Filtering to a common Doppler centroid in the azimuth direction is applied to eliminate the decorrelation due to differences in the Doppler centroid.
- *Coregistration.* In order to obtain the interferometric phase, the image pair has to be coregistered. An accuracy on the subpixel level is needed here.
- *Interferogram formation.* The interferogram is generated by multiplying the first image with the complex conjugate of the second image.
- *Flat-Earth phase removal.* To perform the interferogram noise filtering and simplify the phase unwrapping procedure, a flat-earth phase removal is carried out. The flat-earth phase can be computed by measuring the dominant fringe frequency in the azimuth and range directions of the interferogram.
- *Phase noise reduction.* In order to reduce the phase noise and to facilitate the phase unwrapping, the interferogram is often filtered using an averaging window. After the filtering, the interferometric phase is determined by calculating the arctangent of the interferogram.
- *Coherence image.* The coherence image is computed. The coherence gives information about the quality of the phase measurements.
- *Phase unwrapping.* This operation is necessary because the interferometric phase (unwrapped phase) is only known modulo 2π (wrapped phase). Any procedure which permits the reconstruction of the original unwrapped phase from the wrapped one is called phase unwrapping.

  A large number of algorithms for phase unwrapping is found in the literature. A discussion of different approaches is found in [Bamler and Hartl 98, Gens and van Genderen 96]. Most of the methods are based on the reconstruction of the original phase by integrating its gradient computed from the corresponding wrapped values. [Goldstein et al. 88] used an algorithm

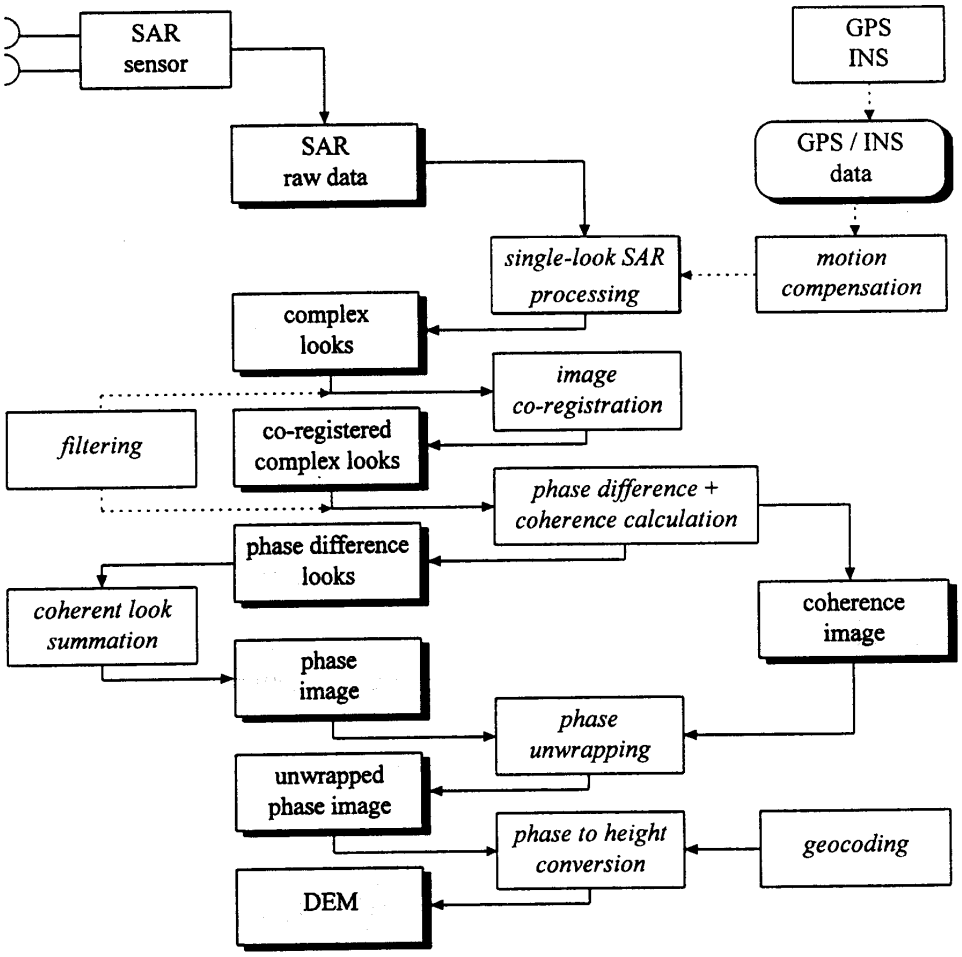

Figure 2: *Processing chain of SAR interferometric data (Gens and van Genderen 96).*

based on the local integration of the phase gradient along a path which connects the image pixels. Different approaches are based on a global integration of the phase gradient.

The phase gradient estimation can be drastically improved in critical areas, i.e., low-coherence areas, if a priori knowledge about the topography is available.

- *Height calculation and geocoding.* The conversion process between the unwrapped phase in slant range and a geocoded DEM is carried out in two steps. The first step is height estimation, that is, calculation of the height values from the interferometric phase information. The resulting height map is given in slant range coordinates. The second step is the geocoding, the transformation onto a carthographic reference system.

  In general, extremely high orbit accuracy is needed to obtain high height accuracy.

2.5 Estimation of terrain height

[Zebker et al. 94] describe how to obtain estimates of the terrain height. Given the two antennas, the surface topography $z(r_g)$ (where r_g is the ground range), and the spacecraft altitude h above a tangent plane to the point of interest, the following equations are used to determine the height:

$$\delta = \frac{\lambda \Delta\phi}{4\pi} \tag{14}$$

$$\sin(\alpha - \theta) = \frac{(r_1 + \delta)^2 - r_1^2 - \mathbf{B^2}}{2r_1\mathbf{B}} \tag{15}$$

$$z(r_g) = h - r_1 \cos\theta \tag{16}$$

where δ is the difference in path lengths, $\Delta\phi$ is the measured interferometric phase, and λ is the wavelength.

This constitutes a recipe for measuring topography with the interferometer. The two principal errors associated with the measurements arise from uncertainties in the measured phase and in the knowledge of baseline. Differentiation of the above equations with respect to $\Delta\phi$ yields the error in height estimate as a function of the error in phase estimate

$$\sigma_z = \frac{\lambda r_1}{4\pi\mathbf{B}} \tan\theta \sigma_{\Delta\phi} \tag{17}$$

where σ_z and $\sigma_{\Delta\phi}$ are the standard deviations of height and phase, respectively.

The second significant error source results from inaccuracies in knowledge of the interferometer baseline alignment. That is, it is impossible to distinguish a baseline angle knowledge error from a slope on the surface topography, and therefore extremely precise knowledge of the baseline geometry is required if absolute height estimation is needed. Differentiation with respect to α yields

$$\sigma_z = r_1 \sin\theta \sigma_\alpha. \tag{18}$$

Note that the error is independent of baseline length and depends only on altitude and range. This is a stringent constraint for spaceborne geometries where the range from the radar to the image swath can be many hundreds of kilometers. This requirements is for absolute accuracy - relative height measurements corrected with ground control points to determine the absolute values do not require this accuracy.

Baseline type	**Interferometric configuration**	**Applications, measurement of ....**
$\Delta\theta$	Single-pass, across-track	topography
Δt = ms to s	Single-pass, along-track	ocean currents moving object detection
Δt = days	Repeat-pass	glacier/ice field, lava flows subsidence seismic events volcanic activities crustal displacements
Δt = ms to years	Repeat-pass, coherence estimator	sea surface decorrelation time scene classification
Δk (frequency)	Δk-radar	exact ranging of targets elimination of propagation medium effects

Table 1: *Possible InSAR configurations (Bamler and Hartl, 1998).*

2.6 Interferometric configurations

The two SAR images forming an interferogram must differ in at least one imaging parameter. The main types of interferometric configurations are [Bamler and Hartl 98]: (i) single-pass, across-track interferometry; (ii) single-pass, along-track interferometry; and (iii) repeat-pass interferometry. These are illustrated in Table 1. [Bamler and Hartl 98] further summarizes the configurations and the applications they are most applicable to.

2.6.1 Across-track interferometry

Across-track interferometry is formed by using a single-pass/dual-antenna arrangement where one antenna (the master) operates in a transmit/receive mode and the slave antenna is in receive mode only. The two antennas are mounted on an axis perpendicular to the flight direction. A thorough description of the principles of operation can be found in [Bamler and Hartl 98]. Since the two images are taken at the same time, temporal decorrelation does not occurre. The only sources of decorrelation are system noise and geometric decorrelation due to spectral shift and volume scattering. The coherence of single-pass interferograms is usually very high (≥ 0.9). Given that the system noise is known, the volumetric scattering contribution can be determined. Single-pass/dual-antenna systems are currently only found on airborne SAR systems.

2.6.2 Along-track interferometry

Along-track interferometry involves two antennas mounted on an aircraft, along the direction of flight. The geometry of along-track systems is similar to across-track system, except that the x-axis and y-axis are exchanged. The phase difference $\Delta\phi$ between two corresponding pixels in the two images is caused by movement of the object, and the velocity of the object can be estimated.

Applications of along-track interferometry are mapping of water currents, detection of moving objects, and measurement of directional wave spectra [Gens and van Genderen 96].

2.6.3 Repeat-pass interferometry

Repeat-pass interferometry requires only one antenna and hence is the method most suited for spaceborne SAR sensors. This is also because the method requires precise location of the flight path, and satellites typically have much more precise and stable paths in the absense of an atmosphere than aircrafts.

2.6.4 Differential interferometry

Differential interferometry can be used to detect small movements of the surface. The principle, which is described in [Gabriel et al. 89], consists of computing an initial interferogram using a pair of radar images taken roughly at the same time. In addition, a second interferogram is created by the use of a third image taken later and combined with one of the original images. These interferograms are unwrapped before computing their difference, which should be a zero phase map unless:

- The specific phase reflection of the terrain was affected by a change of nature (growing vegetation, man-made changes, water content, distortion of the scatterer layout within the resolution cell etc.).
- The atmospheric depth varied randomly within the three scenes.

A more detailed discussion is found in [Massonnet and Rabaute 93].

2.6.5 Interferometry and different SAR system parameters

In addition to the interferometric configuration, other parameters like wavelength and polarization influence the applicability of InSAR for different applications. The baseline required is proportional to the wavelength [Bamler and Hartl 98]. The scattering mechanisms for different cover types depend on the wavelength. Let us consider forest regions as an example. L-band penetrates the vegetation canopy and is reflected from the soil (with double-bouncing from the trunks). C-band is mainly scattered by leaves and branches, while X-band almost does not penetrate the canopy, but gets scattered from its outer boundary. P-band will also to a certain extent penetrate the ground. Temporal decorrelation increases rapidly with frequency, making e.g. L-band more suitable than C- and X-band for repeat-pass InSAR, while single-pass/dual-antenna systems can use higher frequencies.

The height accuracy depends on the wavelength and coherence. For areas with the same coherence for L-, C-, and X-band, the height derived from the X-band phase is approximately two times more accurate than C-band and eight times more than L-band due to the wavelength ratios [Lanari et al. 96].

The polarization is of great influence to the signature of different scatterers. A fully polarimetric SAR can allow separation of different scattering mechanisms, e.g. surface, volume and multiple scattering [Cloude and Pottier 96]. By the use of a theoretical scattering model, [Börner 98] simulated coherence from objects of different scattering classes to study coherence and temporal decorrelation as a function of polarization.

The incidence angle affects the backscatter signature. In addition to the fact that the power decreases with the incidence angle θ, θ should also be chosen as to minimize radar shadow and layover. An incidence angle of about 45° can thus be recommended [Bamler and Hartl 98].

3 Spaceborne and airborne sensors

A number of past, present, and future SAR systems, both airborne and spaceborne, are capable of collecting InSAR data.

3.1 Airborne InSAR systems

Airborne InSARs are particularly useful for regional high-accuracy topography mapping (down to the submeter range) and for ocean current monitoring by along-track systems. Currently, the following systems are operational [Bamler and Hartl 98, Keydell 96, Kramer 96]:

- IFSARE (ERIM/Intermap, USA)
- CCRS C-/X-SAR (Canada Centre for Remote Sensing, Canada)
- EMISAR (Technical University of Denmark)
- Ramses (ONERA, France)
- ESR (DERA, UK)
- DO-SAR (Dornier, Germany)
- E-SAR (DLR, Germany)
- AeS-1 (AeroSensing, Germany)
- AER-II (FGAN, Germany)

3.2 Spaceborne sensors

Past, present and future spaceborne SAR sensors with InSAR capabilities are summarized in Table 2.

3.2.1 SEASAT

SEASAT, the first satellite radar sensor, was operated for 100 days in 1978 (SAR data was collected during 70 days). Some years later, in 1986 and 1989, its interferometry capabilities were demonstrated. [Zebker and Goldstein 86] used it for topographic mapping, while [Gabriel et al. 89] mapped small elevation changes. The orbit determination for SEASAT was not very accurate, making baseline determination a special issue.

3.2.2 SIR-C/X-SAR

The two first space Shuttle Imaging Radar missions, SIR-A (1981) and SIR-B (1984) were essentially copies of the SEASAT SAR and they did not make significant contributions to the field of interferometry. SIR-C/X-SAR, which was flown in April and October 1994, was a big step forward. The October mission had three days dedicated to repeat-pass interferometry by using a 1-day repeat cycle and orbits partially covering the ones from April. One of the most exciting results concerning InSAR was the establishing of a new discipline: polarimetric interferometry [Cloude and Papathanassiou 97, Cloude and Papathanassiou 98, Hellman et al. 97, Papathanassiou and Cloude 97].

Sensor	**Mission period**	**Wavelength polarization**	**Mean incidence angle**	**Remarks**
SEASAT	1978	L, HH	20°	first spaceborne SAR
SIR-C/X-SAR	1994	multipolarization	15-60°	first multifrequency, multipolarization SAR in space
ALMAZ-1	1991-1992	S	30-60°	
ALMAZ-1B	1998	P, S, X multipolarization	25-51°	
ERS-1	1991-today	C, VV	23°	very accurate orbit
ERS-1	1995-today	C, VV		1 day revisit cycle during TANDEM mission
JERS ‡	1992-1998	L, HH	35°	low S/N ratio due to hardware problems
Radarsat	1995-today	C, HH	20-50°	multi-incidence angle multiresolution (10-100 m) ScanSAR option
SRTM	1999	C, X HH,VV	20-60°	dedicated InSAR mission single-pass system standard + ScanSAR modes
ENVISAT	ca. 2000	C HH, VV (VH) alternating	15-45 °	multi-incidence angle very accurate orbit ScanSAR option
LightSAR	ca. 2002	L (possibly C and X) HH, VH, VV, HV	variable 20-45°	short review cycles multi-incidence angle ScanSAR and spotlight option max. resolution 1-3 m

Table 2: Spaceborne SAR systems suitable for interferometry (Bamler and Hartl, 98). ‡ JERS has failed and is no longer in operation.

3.2.3 SRTM

The Shuttle Radar Topography Mission (SRTM) is a cooperative mission between NASA, the US National Imagery and Mapping Agency, the Italian Space Agency, and DLR in Germany. The mission, which will last for 11 days, is scheduled for launch in September 1999. It will cover the Earth between +60 and -58 degrees latitude. The mission will be the first spaceborne single-pass/dual-antenna interferometric system. The goal is to map 80% of the Earth's total landmass. Both C-band and X-band data will be collected, with a horizontal resolution of 30 m and a vertical resolution of 10 m (C-band) and 6 m (X-band). More information is found at the web pages http://www-radar.jpl.nasa.gov/srtm/ and http://www.flr.de/NE-HF/projects/SRTM/SRTM-english.html.

3.2.4 ERS

In the case of satellite sensors, the repeat cycle sets some limitations regarding the applicability of interferometric data. Currently, the ERS satellites have a 35 days repeat cycle. During limited periods, ERS-1 had a 3-day cycle, and ERS-1 and ERS-2 were operated in tandem with a 1-day cycle. These short repeat cycles are very suitable when collecting interferometric data with high coherence (thus suited for generating interferograms or studying changes in areas with low temporal correlation length).

The orbit is determined with decimeter and centimeter accuracy, making the baseline control very good. Most important with respect to interferometry was the tandem mission during which ERS-1 and ERS-2 were operated in parallel. ERS-2 followed ERS-1 on the same orbit with a 35 min delay. In combination with the Earth's rotation, this allowed imaging of the same area and the same look angle at a 1 day time lag. The most serious limitation of the use of interferometric data from ERS is that it uses a steep incidence angle of 23°. This means that terrain slopes of higher than approximately 20° cannot be imaged and makes the system inappropriate for imaging of rugged terrain.

3.2.5 ENVISAT

The next European satellite-borne SAR will be the ASAR on board ENVISAT, currently scheduled for launch in 2000. It will use C-band, but allows a flexibility in alternating between HH, VV and VH polarization. It allows the use of multiple incidence angles and can cover a large swath by using ScanSAR. It will have a repeat cycle of 35 days.

3.2.6 Radarsat

Radarsat, a Canadian satellite, was launched in 1995. It can operate using different incidence angles and different swath widths. Its orbit is not known with very good precision as compared to ERS. The repeat cycle is 24 days. Because of larger range and finer resolution, larger baselines can be tolerated for RADARSAT than ERS [Weydahl 98]. A baseline of 1 km for RADARSAT mode F5 will give similar baseline decorrelation as a 160 m baseline for ERS. Although RADARSAT has poor orbital accuracy, coherence measures and interferometric calculations is feasible when using fine beam mode data with high incidence angles.

4 A survey of applications

InSAR techniques can provide useful information within many application fields. Depending on various factors (e.g., the area under study, the time between repeat acquisitions, the time of year) it is possible to extract very different categories of information. Some of the applications are mutually exclusive (i.e., when a data set is suitable for one application it is unsuitable for another) whereas other applications can extract different signatures from the same data set. At the present time, the major applications of InSAR are:

- DEM generation
- Land-use classification and forest monitoring
- Earthquake risk monitoring
- Monitoring volcanic activity
- Glacier motion measurements

4.1 Land-cover classification

Several studies have demonstrated that the use of InSAR coherence images in combination with backscatter images have improved the separation between various land-cover classes.
[Wegmüller et al. 95] studied the signature of general land-cover classes like water, urban areas, agricultural areas and forest. Urban areas normally showed high coherence values. This was also to a certain extent the case for agricultural fields during the fall/winter when they were bare (given that the soil moisture content did not vary). Forest areas are dominated by volume scattering and will show lower coherence values.

Here, we should add that discrimination between agricultural areas and forest is much simpler based on optical imagery. For map updating purposes, a cloud-free optical image should in most cases be obtainable.

4.2 Crop monitoring

Several studies have shown that the use of coherence in addition to the backscatter values can help in discriminating between various crop types during the growing season.

Engdahl and Borgeaud established a relationship between coherence and agricultural crop height during the early growing season [Engdahl and Borgeaud 98]. They correlated the coherence signature (the time series of coherence measurements) with crop height measurements and established a linear relationship (see Figure 3). However, it was not said how changes in the dielectric constant of the fields due to soil moisture etc. would affect this.

There seems to be a growing interest in modelling the scattering mechanisms for different vegetation types. [Wegmüller et al. 98] present a study where the temporal decorrelation or coherence is modelled in terms of the scattering mechanisms for arid land cover types. They use two different classes of scatterers, temporally stable and temporally unstable scatterers. This type of analysis performed well on arid cover types, for which the dielectric constant is relatively constant.

[Wegmüller and Werner 97] were able to derive the soil moisture from ERS InSAR data from certain agricultural fields. However, they limited their study to bare and sparsely vegetated fields with constant surface roughness to eliminate other sources of decorrelation.

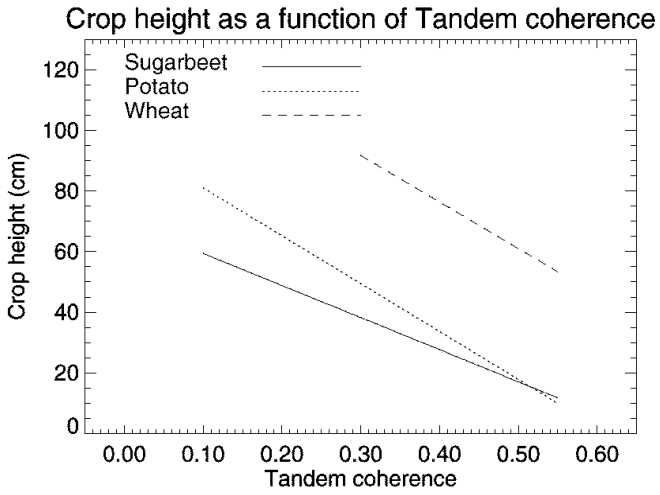

Figure 3: *The relationship between ERS tandem coherence and agricultural crop height during the early growing season (Engdahl and Borgeaud 1998)*

4.3 Forestry

Most of the papers related to forest mapping with InSAR have been related to identifying forest regions and discriminating between forest regions and other land-cover classes (see, e.g., [Strozzi et al. 98a]). The coherence for forested areas is normally low because of the unstable volume scattering from the tree crowns. This has been used to discriminate between forest areas and other areas [Wegmüller 97].

For remote sensing in forestry in Norway, this is not the most interesting task. To be of any real use in forest applications, one must be able to discriminate between various tree species and cutting classes, or derive information like e.g. biomass or tree height for different forest stands.

The interferometric coherence is indirectly related to the forest growth stage through variable ground contribution and tree stiffness under wind influence. If these factors can be controlled, coherence could be used as an indicator of forest biomass [Beaudoin et al. 96]. [Luckman and Baker 97] have studied the relation between coherence and forest biomass for pine stands at Thetford forest in the UK. They found a useful correlation between 1-day repeat coherence and biomass density up to 100 tonnes/hectare. This dependence was stronger than between the backscattering coefficient and biomass density. The coherence in the forest areas over longer time scales were low.

Some work has been directed toward discrimination between various forest types.
[Strozzi and Wegmuller 97] studied discrimination between deciduous, coniferous and mixed forest stands based on coherence. During the winter season, when deciduous stands are without leaves, deciduous forest stands showed larger coherence than coniferous stands. Classification of entire forest stands, i.e. when some segmentation had been used to derive the forest stands, performed reasonably well in forest type discrimination. The results for individual pixels were much worse.

Several studies try to recover tree height or tree crown measurements from InSAR data. Forest canopy height measurements can be extracted in suitable terrain if the coherence is sufficiently high. In general, forested areas exhibit low levels of coherence due to small changes of the individual scatterers due to wind conditions etc. [Hoekman and Varekamp 98] used high-resolution (1.5 m)

airborne InSAR data to study individual trees in tropical rain forests. They found large height errors for individual trees due to layover effects, but they propose a procedure to compensate for this.

[Askne et al. 97] computed the effective tree height from interferometric SAR and compared it to a DEM of the area. They studied ERS-1 interferometric repeat-pass images from a boreal forest area in northern Sweden using data from the three-day repeat cycle period of ERS-1. They presented a scattering model for forested areas useful when deriving tree height measurements. This model includes scattering from the crown, from the soil surface, and from the interaction of the surface and the crown layer or the stem layer. Furthermore, they used the following relation between the tree height and stem volume

$$V = 0.41h^{2.17}, \tag{19}$$

where V is the stem volume and h the height.

The decorrelation has consequences for the effective interferometric tree height. Decorrelation occurs at three different time scales. On the short time scale is the effect of wind moving the scatterers randomly, on the medium scale the dielectric constant changes, e.g., due to precipitation and temperature changes around the ice/water point. On the longer scale is the growth of the vegetation, man made changes, storm damages and fires. The effective tree height is sensitive to the relative fill factor in the area. A change in the decorrelation changes the effective tree height estimated as well as the coherence. They concluded that for good interferometric height measurements of dense forest InSAR observations are best performed at relatively high frequencies when the interferometric effective height is little dependent on the ground surface.

Special considerations are necessary when creating a DEM over forested regions [Engdahl and Hyyppä 97]. A high coherence is needed to achieve accurate DEM results, but the coherence for forest is generally low. [Engdahl and Hyyppä 97] recommend interferograms acquired during the winter season for DEM generation over boreal forest.

4.4 Digital elevation models

Many studies have described the development of interferometric radar systems for highly accurate digital elevation models (DEM) [Graham 74, Zebker et al. 94]. The precision of the technique is now comparable to conventional optical-stereo photogrammetric procedures [Madsen et al. 93].

There are three main approaches to generating topographic data: (i) optical-stereo instruments; (ii) lidar instruments; and (iii) radar interferometry. Spaceborne optical stereo instruments like SPOT can be used to create topographic data with spatial resolutions from 10-30 m and vertical accuracies of 10-20 m [Muller and Eales 90]. Airborne stereo instruments can achieve higher resolution at the cost of the required flight and with a small swath width.

Laser scanners can collect data with a vertical accuarcy of 0.1-1 m. Laser instruments are currently only available as airborne sensors.

Radar interferometry achieves the required resolutions and accuracies without interference from clouds in the atmosphere (but the atmospheric conditions can in certain cases influence the coherence). The DEM generation procedure can, given optimal conditions, be performed without the use of ground control points.

A future alternative to terrain height computation from radar might be to use Spotlight mode stereo SAR images [Desai 97]. This method is analogous to computing height from disparity distance (triangulation) in optical stereo. The height of each scatterer can be estimated from the

radar layover. Stereo SAR is, at first glance, similar to SAR interferometry, in that multiple flight paths is used to produce estimates of height. From an operational perspective, stereo SAR differs in that it is not necessary that the flight paths be nearly identical, in fact, a greater potential for height resolution is gained by using flight paths which have reasonably large separation. To derive height information, the images must lie in different slant planes. The images can be collected from either a single curved flight path or separate flight paths. An elevated scatterer will appear in different range bins, and this difference is used to compute the height estimate. A drawback of this technique is that the scatterers must be visible in both images of the stereo pair. This technique is new, and its potential for height estimation has not yet been fully demonstrated.

Single-pass/dual-antenna SAR systems are easier to use for DEM generation than repeat-pass systems because temporal decorrelation is avoided. However, data from the ERS-1/2 satellites have been extensively used for DEM generation [Hartl 93, Hartl et al. 94, Rufino et al. 98]. Due to the time delay between the two acquisitions the phase of a repeat-pass interferogram contains the following terms:

$$\Delta\phi = \phi_{topo} + \Delta\phi_{prop} + \Delta\phi_{scat} + \Delta\phi_{\delta R} \tag{20}$$

ϕ_{topo} is the wanted topography-induced phase, $\Delta\phi_{prop}$ is a possible phase delay due to ionospheric and atmospheric conditions, $\Delta\phi_{scat}$ is the change in scattering behavior, e.g. due to a change in dielectric constant, $\Delta\phi_{\delta R}$ accounts for displacement of the scatterer.

These terms can be misinterpreted as terrain height unless they are accounted for in the processing. Given optimal conditions, differential interferometry allows mapping of elevation changes at the centimeter level [Gabriel et al. 89, Monti Guarnieri et al. 1992]. In practice, reliable DEM generation from repeat-pass interferometry requires several interferograms (typically 6-10) or the same area [Bamler and Hartl 98]. Depending on the type of terrain and the number of interferograms used accuracies of 5-100 m in height and a spatial resolution of 25 m are typical for ERS interferometry. Single-pass airborne systems can achieve accuracies and resolutions less than a meter.

[Zebker et al. 94] discuss the required resolution for different applications which involved DEM data. Figure 4 illustrates this.

Effect of land cover on the DEM accuracy The accuracy of InSAR DEMs depends on many factors. The factors include the accuracies of such parameters as the slant range, the incidence angle, the baseline and the crossing angle of the two orbits used to create the interferogram. The effect of these parameters on the DEM accuracy can be eliminated if ground control points are used.

The interferometric phase is completely determined by the coherence. The coherence will be affected by temporal scene decorrelation, spatial orbit decorrelation, and radar noise. Since the coherence varies greatly with the land cover type, the land cover type will affect the accuracy of the derived DEM. [Wu et al. 96] found DEM errors for ERS data of less than 4 m vertically for city and rural areas, while for forest areas the errors were up to 14 m.

Frequencies and DEM accuracy The choice of frequency used for DEM construction is a trade off between the height accuracy and the need for high coherence. To get high quality phase estimates, high coherence is needed. This is more easily obtained with lower frequencies, e.g. P- or L-band. On the other hand, the highest accuracy in the height measurements is achieved with higher frequencies, like C-band or X-band. [Lanari et al. 96] combined multifrequency measurements from L-, C- and X-band to create a DEM. The basic shape of the DEM, e.g. the low frequency parts, were derived from L-band data due to its high coherence. The high frequency part of the DEM was derived from C- and X-band data due to their small wavelengths. They

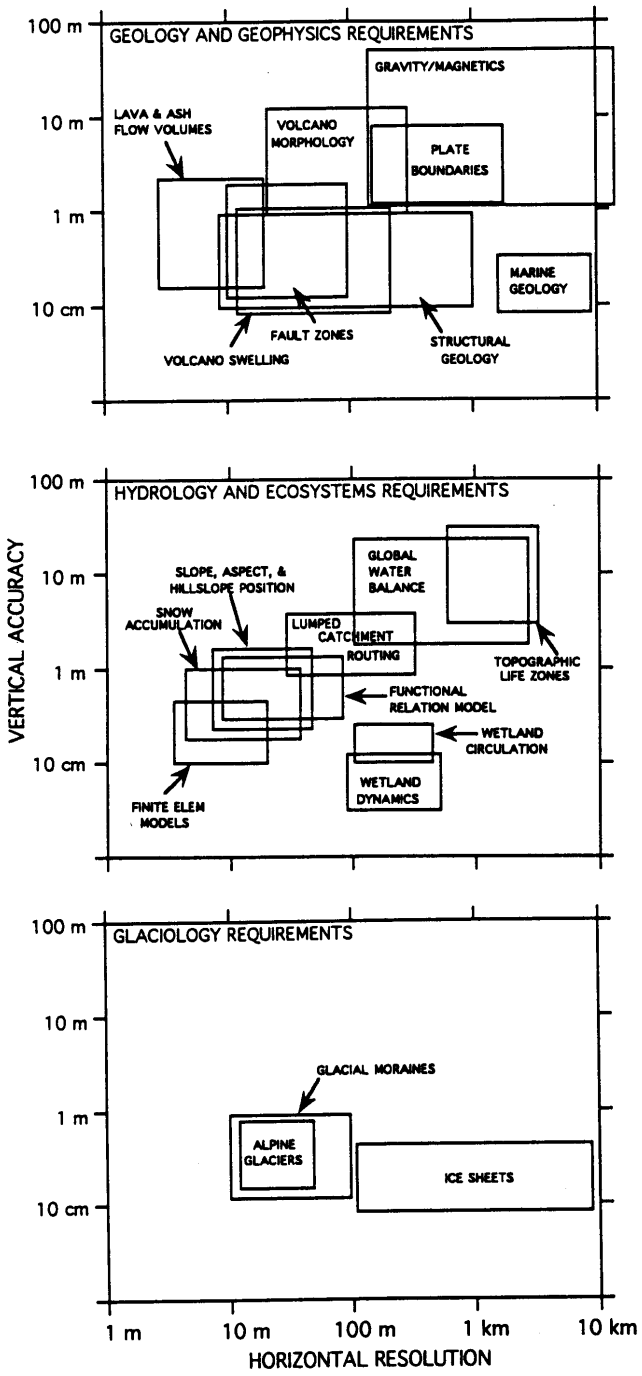

Figure 4: *Graphical depiction of horizontal and vertical topographic data accuracies required for several discipline studies. Each box represents a range of requirements for differing aspects of the studies. (Zebker et al. 1994)*

achieved a height standard deviation of 2.5 m using X-band, 4.5 m using C-band, and 18 m with L-band data.

4.5 Monitoring of snow covered regions

There has been very few approaches to InSAR studies of snow covered regions, perhaps because the snow signature is rapidly changing. [Strozzi et al. 98b] investigated ERS-1 data from the 3-day repeat cycle to study the snow cover of a flat agricultural site in The Netherlands. They found high coherence and similar backscatter intensities for 3-day periods, ecxept during situations with freezing or wet snow. Freezing did not affect the coherence, but changed the backscatter significantly. A drop in coherence was seen when the conditions changed from freezing to thawed. An improvement of using coherence in addition to backscatter values was that the use of coherence enabled distinguishing between wet snow and freeze/thaw conditions. For dry snow, they observed constantly high degrees of coherence and stable backscattering coefficients. During the first warm spring days the decorrelation was slow, but during the warmest spring days it was a very rapid process.

4.6 Glacier motion measurements

InSAR data are used for the measurement of glacier motions and topography changes. This is important for assessing glacier mass transport rates and changes in glacier volume, which in turn is essential for hydrological models. In addition, such information can have significant implications for global climate change assessment.

Norwegian Polar Institute and NDRE have cooperated in analysing ERS tandem data from Kronebreen glacier at Svalbard [Eldhuset et al. 96]. By using an existing DEM in combination with an InSAR derived DEM, they were able to monitor motion of the fast moving glacier (see Figure 5). For this purpose, 1 day interval tandem data was essential. They were also able to detect errors in existing DEMs.

Another application of interferometry in regions with ice cover is the monitoring of aufeis in rivers. Aufeis deposits, which are also called overflow ice, stream icings or naleds, develop on many rivers in high latitudes and in alpine regions. The presence of aufeis in a drainage basin tends to stabilize river discharge in the same way as a glacier does, by providing melt water during hot dry periods. The distribution of aufeis deposits along the rivers is discontinuous because of variations in channel geometry and under-ice water supply, and monitoring their growth during the winter is important. [Li et al. 97] achieved promising result in monitoring aufeis with ERS InSAR data.

[Unwin and Wingham 96] combined three ERS-1 images from the 3-day repeat cycle period to derive both topographic and velocity information. They found data sets separated by more than 6 days to have too low coherence. They assumed the coherence loss to be due to precipitation in the form of snow. They achieved a vertical accuracy of the topographic data of 8 m.

4.7 Flood monitoring

Flooding may lead to severe damage of the land surrounding the river. [Izenberg et al. 96] used InSAR data to study the Missouri River floods in 1993. The river is surrounded by agricultural regions, which were damaged by massive amounts of sand carried by the floodwater and deposited on top of the fields. They used SIR-C data in combination with a canopy scattering model to study the field after the flooding. They also used a DEM created from TOPSAR data of the

ERS-1 SAR image (ESA)

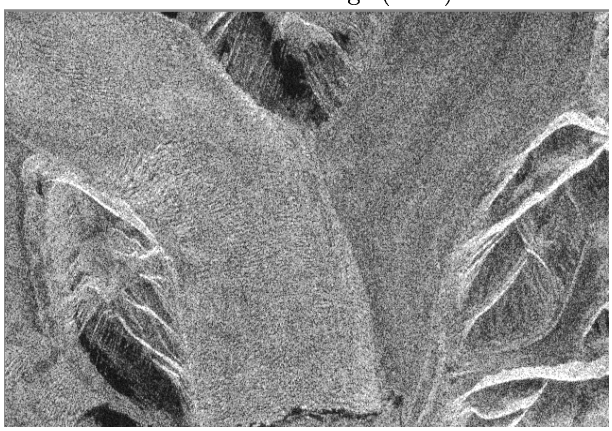

ERS-1/ERS-2 interferogram (NDRE)

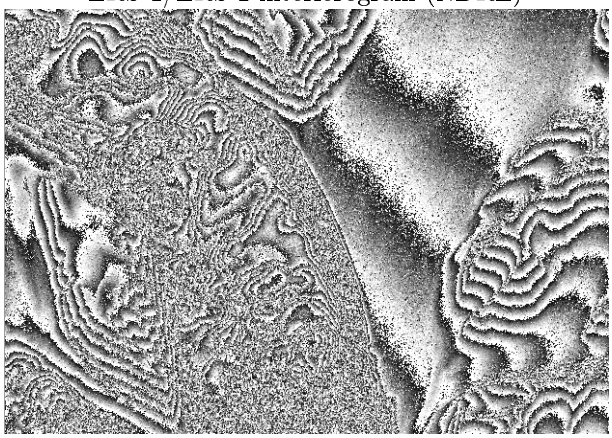

Interferogram where the terrain fringes have been removed (NDRE)

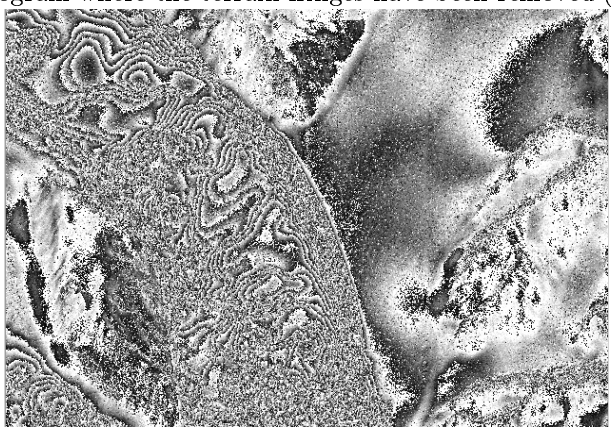

Figure 5: *ERS-1 SAR image from Kronebreen (from Eldhuset et al. 96).*

flooded area. The DEM had a vertical accuracy of 1 to 2 m, which provided enough accuracy to estimate the total mass removed during erosion and scour of the bottoms terrains.

[Geudtner et al. 96] studied ERS-1 SAR image pairs from the 3-day repeat cycle from the 1993/94 Rhine river flood event. They found that using coherence in addition to backscatter allowed identification of the flooded areas significantly better than using only the backscatter values, particularly in regions with high backscatter values.

4.8 Geophysical hazard analysis

Monitoring of areas with high risk of earthquakes, volcanic activity or land subsidience require the use of differential interferometry, in which very small land surface movements can be detected.

4.8.1 Earthquake risk monitoring

The potential of radar interferometry for earthquake deformation was demonstrated on the 1992 earthquake in Landers, California on 28 June 1992 [Massonnet 96]. ERS-1 images were acquired on four different dates: 24 April, 3 July, 7 August and 11 September. The 24 April - 7 August pair provided the optimum conditions for interferometry. Field and seismological investigations were used to build a model of the surface displacements. The ERS-1 derived displacements fitted very well with the model.

For deep earthquakes associated with little or no surface rupture, radar interferometry has become a powerful tool for measuring surface displacement. Unlike surveying techniques, there is no need to install ground stations before the earthquake, a major point in terms of cost. To ensure a pre-earthquake observation, one only needs to archive radar images of the potentially seismogenic area. Several earthquakes have now benefit from the technique.

Under ideal conditions, radar interferometry can measure displacements of 3 to 10 centimeter along a swath of 50 to 100 km wide. For tectonic studies, these data are providing a wealth of new understanding compared to the sparsely recordings of GPS networks.

4.8.2 Monitoring of volcanic activity

Volcano deformation is another field where monitoring by spaceborne interferometry holds promise for complementing the costly and often hazardous installation and maintenance of an instrument network.

The Mount Etna eruption, which started in December 1991 and ended in March 1993 has been used to document the performance of interferometry to measure deformation [Massonnet 96]. A total of 29 ERS-1 images from both ascending and descending passes were processed. Volcano-wide deformation were revealed and associated volume change measured.

Continuing work on other volcanoes, like the Merapi volcano in Indonesia, has shown that it is possible to obtain results even in equatorial areas, where rapid surfaces changes occur owing to lush vegetation.

4.9 Geological applications

In certain areas of the world, the geological structures lie on the surface of the earth. For these areas, interferometry can be used for oil exploration purposes or mapping of mineral resources. Oil field subsidience monitoring, the monitoring of surface deformation at the millimeter level, is important in areas with hydrocarbon production. InSAR applied to this task is studied by [Biegert et al. 98].

[Ichoku et al. 98] studied the use of coherence images in combination with amplitude images to enhance geological structures. They achieved good result for visual interpretation purposes by applying a principal component transform to a combination of amplitude and coherence images.

4.10 Other applications

In many areas, like the US or Siberia, pipelines for oil and gas are placed on the land surface. These pipelines are the object of movements of either the surface cover or the pipeline itself, which might lead to cracks and severe damage. These problems require a permanent monitoring of existing and a careful planning of new pipeline tracks. Planning information such as a DEM and a classification of the surface is usually derived from optical remote sensing and field work. [Streck and Wegmüller 97] investigated the potential or using ERS SAR data for this purpose. Currently, pipelines are monitored by visual inspection from a helicopter. SAR data proved to be a valuable alternative for the mapping of pipelines.

5 Case study: analysis of Radarsat images from Heimdalen

An analysis of RADARSAT images from Heimdalen in Jotunheimen was performed to get some experience with InSAR data. Six RADARSAT Single-Look Complex images acquired during the snow melting season in 1997 (from the SNOWTOOLS project) were available.

The test area is located near the lake Heimdalsvatnet, Norway, 61 degrees 25' N, 9 degrees E. Three RADARSAT images from Standard Mode S7 (with incidence angles from 45-49 degrees) from April 24, May 18, and June 11 1997, and three images from mode S2 (incidence angle 24-31 degrees) from April 25, May 19, and June 12 were available.

We have not seen many successful approaches to InSAR for snow monitoring applications in the literature. Snow is a medium with low coherence, and thus difficult to use for InSAR applications. This experiment was performed to gain experience with coherence images, and the data set was chosen because it was the only SLC data set we had access to. We also wanted to see if we could get any useful information from the SAR coherence images.

The six images are shown in Figures 6-7. The pixel spacing in range is 11.5 m, and 5 m in azimuth. The images were delivered as ordinary SLC images, that is, they were not processed for InSAR use (e.g. with a common Doppler centroid). We can thus not use the interferograms, and even for the coherence images this sets limits. Because of the use of two different Doppler centroids and the topography, the coherence will be limited. For InSAR applications, image pairs with the same incidence angles must be used, e.g. April 24 and May 18, April 25 and May 19, May 18 and June 11, or May 19 and June 12.

The snow is in April estimated to be dry. The temperature in the area was well below freezing during the satellite passes, which were around 5 PM. In May, the snow froze during the night, but melted during the day as it was sunny. In June, the snow was very wet, and it did not freeze during the night.

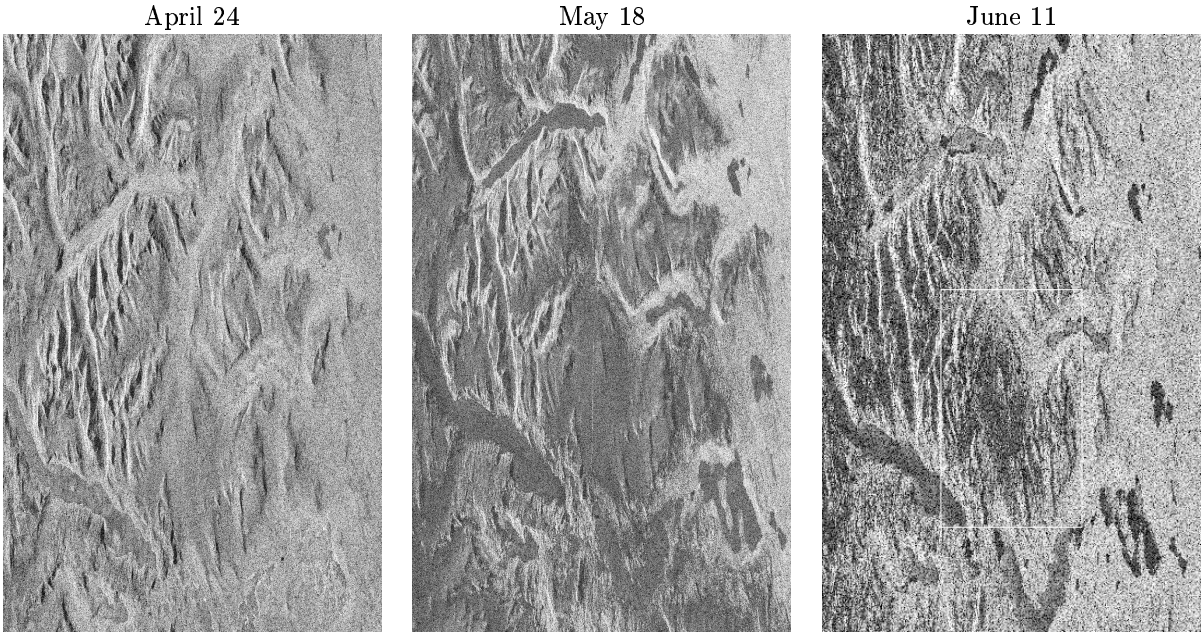

Figure 6: *RADARSAT backscatter images (mode S7) from April 24, May 18, and June 11, 1997 from Heimdalen. Note that the pixel spacing is 5 m in azimuth and 11.5m in range.*

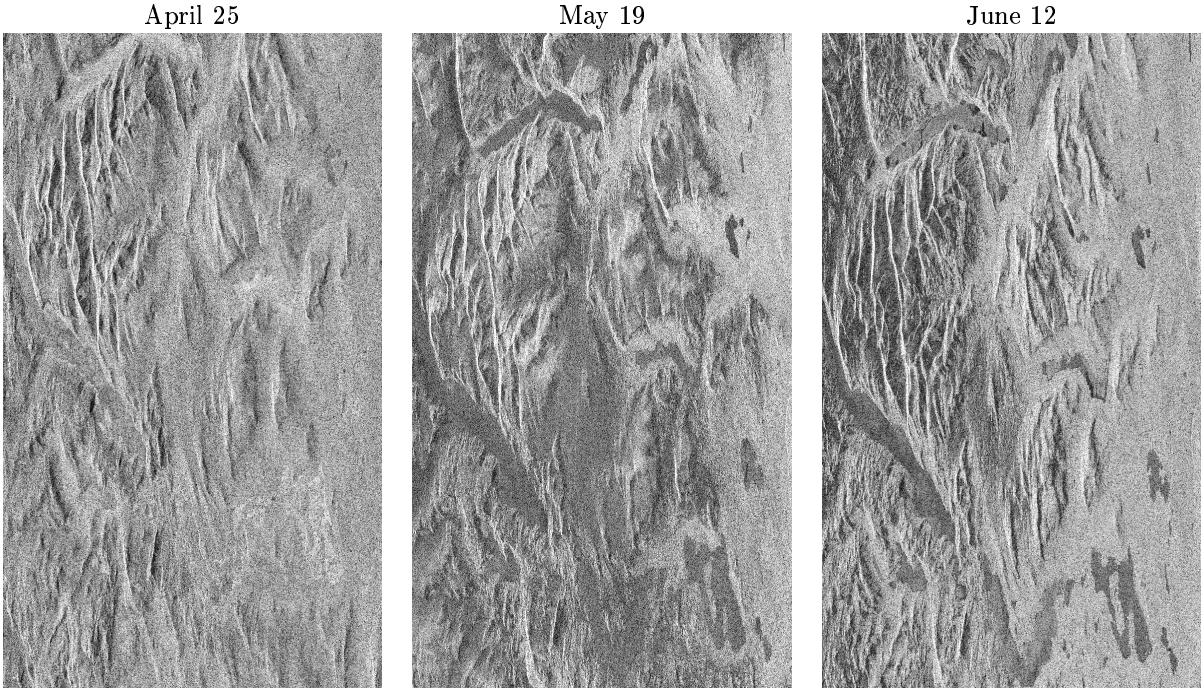

Figure 7: *RADARSAT backscatter images (mode S2) from April 25, May 19, and June 12, 1997 from Heimdalen.*

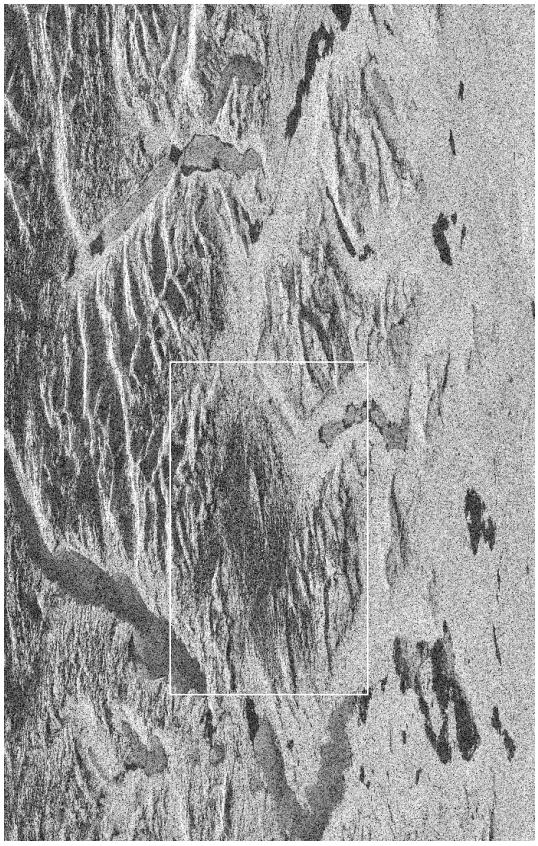

Figure 8: *Location of the subarea selected for further processing.*

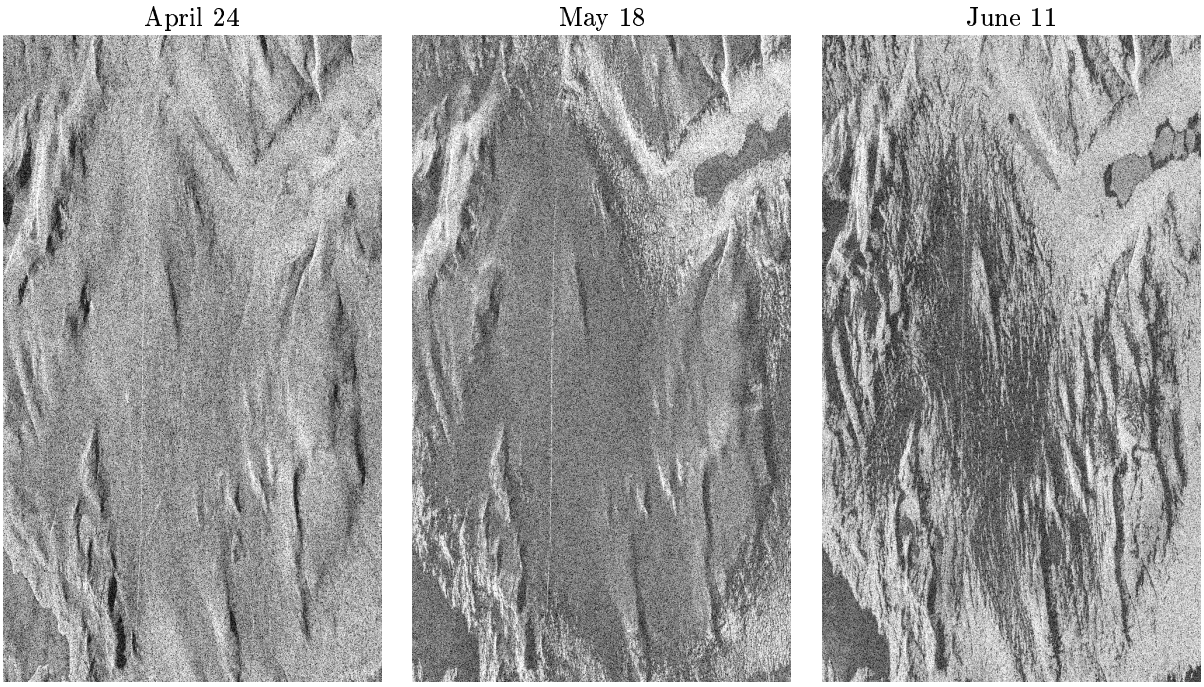

Figure 9: *Backscatter subimages from April 24, May 18, and June 11, 1997 from Heimdalen.*

A subimage consisting of the Valdresflya area (as indicated in Figure 8) was selected for further analysis. The subimages for April 24, May 18, and June 11 are shown in Figure 9.

The RADARSAT SLC images are stored in two-band images, where band one contains the real part, I, and band two the imaginary part, Q. A backscatter image in dB can be formed using the transform $10 \log_{10}(I^2 + Q^2)$.

To estimate the coherence, a rectangular window is often used. Since the pixel spacing in range and azimuth is different, a larger window in azimuth than range is used. We used a window of 3×15 (range, azimuth). The azimuth pixel size in the resulting coherence image will be $15 \times \text{AzimuthPixelSpacing} = 15 * 5\ m = 75\ m$, while the average pixel size in range will be $3 \times \text{RangePixelSpacing}/\sin(\text{IncidenceAngle}) = 3 \times 11.5\ m/\sin(45) = 50\ m$.

Ideally, we could have computed the baseline and $\gamma_{Baseline}$ (the baseline decorrelation) between the image pairs. Because we did not have access to orbit data (including the positions of the satellites), we could not do this. Our analysis was also limited by the fact that we did not have access to any InSAR software product.

Image coregistration is necessary for coherence computation. We did this using a two-step process to avoid resampling of the original data. First, we manually found the location of the subimage, for each SAR image, which covered the area of interest, as good as possible. This accounts for a general shift of the positions of the different images, but not for local distortions. After the first step was applied to an image pair, we observed local mismatches in the size of 2-3 pixels. The second step, which was performed during the coherence computations, accounted for local mismatches in the following manner: For each pixel in image A, the coherence was computed for a set of pixel positions in image B by shifting the position of the window by $\pm k$ ($k = 5$ was used) pixels in both range and azimuth. Then the maximum coherence found among the shifted windows was used as the coherence value.

The coherence was computed for the images from May 18 and June 11. The coherence image is

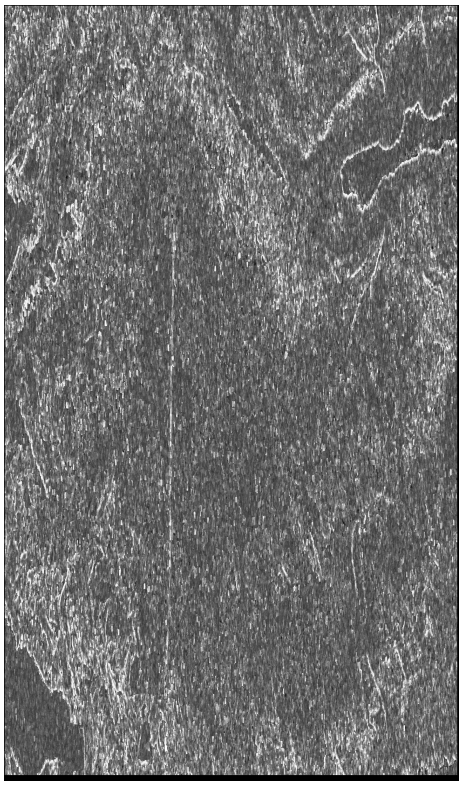

Figure 10: Coherence image for the 18 May/11 June image pair.

shown in Figure 10. The coherence is generally low. Only certain structures, like the road across Valdresflya and the borders of the lakes Heimdalsvatnet and Bygdin, have higher coherence values than the surroundings. From this image pair, which is separated by 24 days, there seems to be little information to gain with respect to the snow conditions. As expected, to monitor snow during the melting season image pairs with short revisit cycles are needed. InSAR image pairs processed to a common Doppler centroid and knowledge about the topography should also have been used to fully study the potential for snow monitoring applications.

6 Conclusions

We have briefly reviewed the basic principles of radar interferometry. The purpose was to provide enough details to be able to understand the requirements and potential for different applications, without presenting the theory in depth.

Both airborne and spaceborne sensors collect InSAR data. Most airborne systems are dual-antenna systems, which collect an image pair using two antennas and a single pass over the area. There is no decorrelation due to temporal changes on the ground, and the data from single-pass/dual-antenna systems is well suited for topography applications.

Satellite sensors are so far only capable of repeat-pass interferometry. The first spaceborne dual-antenna InSAR system will be the Shuttle Radar Topography Mission, which is scheduled for September 2002. The repeat cycle of the sensor limits the applicability of the data for some applications, mainly due to decorrelation. An advantage of spaceborne systems is the large swath width and the stable orbits.

The ERS satellites, and in particular the tandem mission and the 3-day repeat cycle period of ERS-1, have boosted the number of applications of InSAR data. This will probably continue with Radarsat and ENVISAT, although they have repeat cycles of 24 and 35 days. A very interesting sensor is LightSAR, which is scheduled for launch in 2002. The repeat cycle can be altered from 8 days for a particular area to 24 days for all areas. LightSAR will have high-priority goals of refined understanding of earthquakes, volcanoes and other natural hazards.

The major applications of InSAR are DEM generation, land-use classification and forest monitoring, earthquake risk monitoring, monitoring of volcanic activity, and glacier monitoring.

One of the most important applications is generation of digital elevation models. Given optimal conditions, differential interferometry allows mapping of elevation changes at the centimeter level. Single-pass/dual-antenna systems have the potential of achieving higher precision in terrain height measurements than repeat-pass systems. The Shuttle Radar Topography Mission, scheduled for 1999, is expected to achieve a height accuracy of 6 m using X-band and 10 m using C-band. In practice, the accuracies reported for spaceborne sensors vary from 5-100 m in height depending on the type of terrain, the conditions, and the number of interferograms used.

In general land-cover classification, InSAR coherence images have been a useful supplement to backscatter images to discriminate general land-cover classes. Most of the InSAR papers related to forestry have been focused on discrimination between forest regions and other regions based on coherence. More interesting for practical forestry applications is the recovery of tree height or tree crown measurements from InSAR data. This is an active research area, but more research is needed before the theory can be used for operational applications.

InSAR data are used for the measurement of glacier motions and topography changes. This is important for global climate change assessment and as input to hydrological models.

A very promising application of differential interferometry is monitoring of geophysical hazards. Differential interferometry can detect very small land surface movements. For both earthquake risk monitoring and monitoring of volcanic activity, interferometry has proved to provide valuable data to complement the costly and often hazardous installation and maintenance of a network of field sensors. So far, InSAR data have been compared to data from field measurements and existing models, and promising results have been reported for monitoring of both earthquake risk and volcanic risk or activity.

To summarize, radar interferometry is a rapidly developing field. The number of applications is growing. Interferometry opens up new applications for which remote sensing data have previously not been applied successfully to. More research is needed for operational use of interferometric data for most applications.

References

[Askne and Hagberg 93] Askne, J. and Hagberg, J.O., 1993, Potential of interferometric SAR for classification of land surfaces. Proceedings of IGARSS '93, Tokyo, Japan, 985-987.

[Askne et al. 97] Askne, J.I.H., Dammert, P.B.G., Ulander, L.M.H. and Smith, G., 1997, C-Band Repeat-Pass Interferometric SAR Observations of the Forest. *IEEE Transactions on Geoscience and Remote Sensing,* vol. 35, 25-35.

[Bamler and Hartl 98] Bamler, R. and Hartl, P., 1998, Synthetic aperture radar interferometry, *Inverse Problems,* 14, R1-R54.

[Beaudoin et al. 96] Beaudoin, A., Castel, Th. and Rabaute, Th., 1996, Forest monitoring over hilly terrain using ERS INSAR data. ESA Fringe'96 Workshop, Zurich, Switzerland. See http://www.geo.unizh.ch/rsl/fringe96/papers/.

[Biegert et al. 98] Biegert, E., Berry, J., and Oakley, S. 98. Oil field subsidence monitoring using spaceborne interferometric SAR. See http://www.atlsci.com/library/papers/Oil_field_ Subsidence _Monitoring_using_Spaceborne _Interferometric_SAR.html.

[Börner 98] Börner, T, 1998, Coherent modeling of vegetation for polarimetric SAR interferometry applications, Retrieval of Bio- and Geo-Physical Parameters from SAR Data for Land Applications Workshop, ESTEC, 21-23 October 1998. See http://www.estec.esa.nl/CONFANNOUN/98c07/.

[Cloude and Papathanassiou 98] Cloude, S. R. and Papathanassiou, K. P., 1998, Polarimetric SAR interferometry, *IEEE Transactions Geoscience and Remote Sensing,* 36, 1551-1565.

[Cloude and Papathanassiou 97] Cloude, S. R. and Papathanassiou, K. P., 97, Coherence optimisation in polarimetric SAR interferometry. Proceedings of IGARSS'97, Singapore, 1932-1934.

[Cloude and Pottier 96] Cloude, S. R. and Pottier, E., 1996, A review of target decomposition theorems in radar polarimetry, *IEEE Transactions Geoscience and Remote Sensing,* 34, 498-518.

[Desai 97] Desai, M., 97. Spotlight mode SAR stereo technique for height computation, *IEEE Trans. Image Processing,* vol. 6, 1400-1411.

[Eldhuset et al. 96] Eldhuset, K., Aanvik, F., Aksnes, K., Amlien, J., Andersen, P.H., Hauge, S., Isaksson, E., Wahl, T. and Weydahl, D.J., 1996, First results of ERS tandem INSAR processing on Svalbard. ESA Fringe'96 Workshop, Zurich, Switzerland. See http://www.geo.unizh.ch/rsl/fringe96/papers/.

[Engdahl and Hyyppä 97] Engdahl, M. and Hyyppä, J., 1997, Forest inventory using interferometric SAR techniques. Proceedings of the Third ERS Symposium, Florence, Italy. See http://earth1.esrin.esa.it/florence/papers/.

[Engdahl and Borgeaud 98] Engdahl, M., and Borgeaud, M., 1998, ERS-1/2 tandem interferometric coherence and agricultural crop height, Retrieval of Bio- and Geo-Physical Parameters from SAR Data for Land Applications Workshop, ESTEC, 21-23 October 1998. See http://www.estec.esa.nl/CONFANNOUN/98c07/.

[Evans et al. 92] Evans, D.L., Farr, T.G., Zebker, H.A. and Mouginis-Mark, P.J., 1992, Radar interferometry studies of the earth's topography, *EOS, Transactions, American Geophysical Union,* 73, 553, 557-558.

[Gabriel and Goldstein 88] Gabriel, A.K. and Goldstein, R.M., 1988, Crossed orbit interferometry: theory and experimental results from SIR-B, *International Journal of Remote Sensing*, 9, 857-872.

[Gabriel et al. 89] Gabriel, A.K., Goldstein, R.M. and Zebker, H.A., 1989, Mapping small elevation changes over large areas: Differential radar interferometry. *Journal of Geophysical Research,* 94 (B), 9183-9191.

[Gatelli et al. 94] Gatelli, F., Monti Guarnieri, A., Parizzi, F., Pasquali, P., Prati, C. and Rocca, F., 1994, The Wavenumber Shift in SAR Interferometry. *IEEE Transactions on Geoscience and Remote Sensing,* 32, 855-864.

[Gens and van Genderen 96] Gens, R. and Genderen, J.L. van, 1996, SAR interferometry - issues, techniques, applications. *International Journal of Remote Sensing,* 17, 1803-1835.

[Geudtner et al. 96] Geudtner, D., Winter, R. and Vachon, P.W., 1996, Flood Monitoring Using ERS-1 SAR Interferometry Coherence Maps. Proceedings of IGARSS '96, Lincoln, Nebraska, 966-968.

[Goldstein et al. 88] Goldstein, R.M., Zebker, H.A. and Werner, C.L., 1988, Satellite radar interferometry: Two-dimensional phase unwrapping. *Radio Science,* 23, 713-720.

[Goldstein et al. 89] Goldstein, R.M., Barnett, T.P. and Zebker, H.A., 1989, Remote Sensing of Ocean Currents. *Science*, 246, 1282-1285.

[Goldstein and Zebker 87] Goldstein, R.M. and Zebker, H.A., 1987, Interferometric radar measurement of ocean surface currents. *Nature*, 328, 707-709.

[Graham 74] Graham, L.C., 1974, Synthetic Interferometer Radar for Topographic Mapping. *Proceedings of the IEEE*, 62, 763-768.

[Hartl 93] Hartl, Ph., 1993, Radar Interferometry - Basic concept and applications -. Proceedings of ISPRS Workshop and Conference International Mapping from Space, Hannover, Germany, 207-232.

[Hartl et al. 94] Hartl, Ph., Thiel, K.-H. and Wu, Y.X., 1994, Practical application of SAR interferometry: experience made by the institute of navigation. Proceedings of the Second ERS-1 Symposium, Hamburg, Germany, 717-722.

[Hellman et al. 97] Hellman, M., Cloude, S. R., and Papathanassiou, K. P., 97, Classification using polarimetric and interferometric SAR-data, Proceedings of IGARSS'97, Singapore, 1411-1413.

[Hoekman and Varekamp 98] Hoekman, D., and Varekamp, C., 98, High resolution single-pass interferometric radar observation of tropical rain forest trees. Retrieval of Bio- and Geophysical Parameters from SAR Data for Land Applications Workshop, ESTEC, October 1998. See http://www.estec.esa.nl/CONFANNOUN/98c07/.

[Ichoku et al. 98] Ichoku, C., Karnieli, A., Arkin, Y., Chorowicz, J., Fleury, T., and Rudant, J., 98. Exploring the utility potential of SAR interferometric coherence images. *International Journal of Remote Sensing,* vol. 19, 1147-1160.

[Izenberg et al. 96] Izenberg, N., Arvidson, R., Brackett, R., Saatchi, S., Osburn, G., and Dohrenwend, J., 96. Erosional and depositional patterns associated with the 1993 Missouri River floods inferred from SIR-C and TOPSAR radar data. *Journal of Geophysical Research,* vol. 101, 23149 - 23167.

[Kramer 96] Kramer, H. J., 1996, *Observation of the Earth and its Environment,* Berlin, Springer.

[Keydell 96] Keydell, W., 1996, SAR technique and technology, its present state of the art with respect to user requirements, Proceedings of EUSAR'96, Koningswinter, 19-24.

[Lanari et al. 96] Lanari, R., Fornaro, G., Riccio, D., Migliaccio, M., Papathanassiou, K.P., Moreira, J.R., Schwäbisch, M., Dutra, L., Puglisi, G., Franceschetti, G. and Coltelli, M., 1996, Generation of Digital Elevation Models by Using SIR-C/X-SAR Multifrequency Two-Pass Interferometry: The Etna Case Study. *IEEE Transactions on Geoscience and Remote Sensing,* 34, 1097-1115.

[Lee et al. 94] Lee, J.-S., Hoppel, K.W., Mango, S.A. and Miller, A.R., 1994, Intensity and phase statistics of multilook polarimetric and interferometric data. *IEEE Transactions on Geoscience and Remote Sensing,* 32, 1017-1027.

[Li et al. 97] Li, S., Benson, C., Shapiro, L, and Dean, K., 1997. Aufeis in the Ivishak River, Alaska, Mapped from Satellite Radar Interferometry. *Remote Sensing of Environment,* vol, 60, 131-139.

[Luckman and Baker 97] Luckman, A. and Baker, J., 1997, Interferometric coherence measurements of tropical, temperate and boreal forests. Proceedings of the Third ERS Symposium, Florence, Italy. See http://earth1.esrin.esa.it/florence/papers/.

[Madsen et al. 95] Madsen, S.N., Martin, J.M. and Zebker, H.A., 1995, Analysis and Evaluation of the NASA/JPL TOPSAR Across-Track Interferometric SAR System. *IEEE Transactions on Geoscience and Remote Sensing,* 33, 383-391.

[Madsen et al. 93] Madsen, S.N., Zebker, H.A. and Martin, J., 1993, Topographic mapping using radar interferometry: processing techniques. *IEEE Transactions on Geoscience and Remote Sensing*, 31, 246-256.

[Massonnet and Rabaute 93] Massonnet, D. and Rabaute, T., 93. Radar interferometry: limits and potential. *IEEE Transactions on Geoscience and Remote Sensing,* vol. 31, 455-464.

[Massonnet 96] Massonnet, D., 1996, Tracking the Earth's surface at the centimetre level: an introduction to radar interferometry. *Nature & Resources,* vol. 32, 20-29.

[Monti Guarnieri et al. 1992] Monti Guarnieri, A., Parizzi, F., Pasquali, P., Prati, C. and Rocca, F., 1992. Developments in ERS-1 SAR interferometry, Proceedings of 1st ESA ESRIN Workshop, Frascati, Italy, pp. 13.

[Monti Guarnieri and Prati 97] Monti Guarnieri, A. and Prati, C., 1997, SAR Interferometry: A "Quick and Dirty" Coherence Estimator for Data Browsing. *IEEE Transactions on Geoscience and Remote Sensing,* 35, 660-669.

[Moreira et al. 95] Moreira, J., Schwäbisch, M., Fornaro, G., Lanari, R., Bamler, R., Just, D., Steinbrecher, U., Breit, H., Eineder, M., Franceschetti, Geudtner, D. and Rinkel, H., 1995, X-SAR Interferometry: First Results. *IEEE Transactions on Geoscience and Remote Sensing,* 33, 950-956.

[Muller and Eales 90] Muller, J.-P. and Eales, P., 1990, Global topography accuracy requirements for EOS, Proceedings of IGARSS'90, Washington, DC, 1411-1414.

[Papathanassiou and Cloude 97] Papathanassiou, K. P. and Cloude, S. R., 1997, Polarimetric effects in repeat-pass SAR interferometry, Proceedings of IGARSS'97, Singapore, 1926-1928.

[Richman 71] Rickman, D. *Three Dimensional Azimuth-correcting Mapping Radar*, United Technologies Corporation, USA, 1971.

[Rosen et al. 96] Rosen, P.A., Hensley, S., Zebker, H.A., Webb, F.H. and Fielding, E., 1996, Surface deformation and coherence measurements of Kilauea Volcano, Hawaii from SIR-C radar interferometry. *Journal of Geophysical Research,* 101 (E10), 23,109-23,125.

[Rufino et al. 98] Rufino, G., Moccia, A. and Esposito, S., 1998, DEM Generation by Means of ERS Tandem Data, *IEEE Tr. Geoscience Remote Sensing,* vol. 36, 1905-1912.

[Streck and Wegmüller 97] Streck, C., and Wegmüller, U., 97. Investigation of ERS SAR data of the tandem mission for planning and monitoring of Siberian pipeline tracks. Proceedings of the Third ERS Symposium, Florence, Italy. See http://earth1.esrin.esa.it/florence/papers/.

[Strozzi and Wegmuller 97] Strozzi, T. and Wegmüller, U., 1997, Forest mapping with ERS SAR interferometry. Proceedings of the Third ERS Symposium, Florence, Italy. See http://earth1.esrin.esa.it/florence/papers/.

[Strozzi et al. 98a] Strozzi, T., Dammert, P., Wegmüller, U., Martinez, J., Beaudoin, A., Askne, J., and Hallikainen, M., 98. European Forest Mapping with SAR interferometry. Retrieval of Bio- and Geophysical Parameters from SAR Data for Land Applications Workshop, ESTEC, October 1998. See http://www.estec.esa.nl/CONFANNOUN/98c07/.

[Strozzi et al. 98b] Strozzi, T., Wegmüller, U., and Mätzler, C., 98. Using repeat-pass SAR interferometry for mapping wet snowcovers. Proceedings of IGARSS'98, Seattle, Washington, 1650-1652.

[Unwin and Wingham 96] Unwin, B. and Wingham, D., 1996, Topography and Dynamics of Austfonna, Svalbard, from SAR Interferometry. ESA Fringe'96 Workshop, Zurich, Switzerland. See http://www.geo.unizh.ch/rsl/fringe96/papers/.

[Wegmüller et al. 95] Wegmüller, U., Werner, C.L., Nüesch, D. and Borgeoud, M., 1995, Land-Surface Analysis Using ERS-1 SAR Interferometry. *ESA bulletin*, No. 81, 30-37.

[Wegmüller and Werner 97] Wegmüller, U. and Werner, C., 1997, Retrieval of Vegetation Parameters with SAR Interferometry. *IEEE Tr. Geoscience Remote Sensing,* vol. 35, 18-24.

[Wegmüller 97] Wegmüller, U., 1997, Soil moisture monitoring with ERS SAR interferometry. Proceedings of the Third ERS Symposium, Florence, Italy. See http://earth1.esrin.esa.it/florence/papers/.

[Wegmüller et al. 98] Wegmüller, U., Strozzi, T., Farr, T., and Werner, C., 98. Arid land surface characterization with repeat-pass SAR interferometry. Retrieval of Bio- and Geophysical Parameters from SAR Data for Land Applications Workshop, ESTEC, October 1998. See http://www.estec.esa.nl/CONFANNOUN/98c07/.

[Weydahl 98] Weydahl, D. J., 1998, Analysis of satellite SAR images for change detection over land areas, Ph.D. thesis, Department of Geography, University of Oslo, Norway.

[Wu et al. 96] Wu, X., Thiel, K.-H. and Wehr, A., 1996, The effects of different land covers on the accuracy of the interferometric DEMS. ESA Fringe'96 Workshop, Zurich, Switzerland. See http://www.geo.unizh.ch/rsl/fringe96/papers/.

[Zebker et al. 94] Zebker, H.A., Werner, C.L., Rosen, P.A. and Hensley, S., 1994, Accuracy of topographic maps derived from ERS-1 interferometric radar. *IEEE Transactions on Geoscience and Remote Sensing,* 32, 823-836.

[Zebker and Goldstein 86] Zebker, H.A. and Goldstein, R.M., 1986, Topographic Mapping From Interferometry Synthetic Aperture Radar Observations. *Journal of Geophysical Research,* 91 (B5), 4993-4999.